https://doi.org/10.1016/j.optlastec.2022.108865

Creating anisotropic topological phases within inversely designed photonic crystals

Yafeng Chen[1,2], Zhihao Lan[3†], Jie Zhu[4*], and Zhongqing Su[2§]

[1]*State Key Laboratory of Advanced Design and Manufacturing for Vehicle Body, Hunan University, Changsha, Hunan 410082, P. R. China*

[2]*Department of Mechanical Engineering, Hong Kong Polytechnic University, Hong Kong SAR, P. R. China*

[3]*Department of Electronic and Electrical Engineering, University College London, London WC1E 7JE, United Kingdom*

[4]*School of Physics Science and Engineering, Tongji University, Shanghai 200092, P. R. China*

Abstract

Photonic topological insulators endow flexible manipulation of light with high efficiency and robustness. The majority of previous research concentrated on isotropic topological states, with anisotropic topological states receiving less attention. In this study, we investigate anisotropic topological edge states in two-dimensional photonic systems for both the transverse magnetic (TM) and transverse electric (TE) modes. First, using the topology optimization method, photonic crystals (PCs) with maximized odd-order band gaps, from the first-order to the seventh-order, are created. An anisotropic topological phase transition is then obtained by shifting the primitive unit cell (UC) of the optimized PC along the horizontal direction by half of the lattice constant. Tightly localized anisotropic topological edge states are thus formed at the interface between the primitive and translated UCs. Finally, the transmission properties of the anisotropic topological edge states are numerically demonstrated. Our findings could aid in the development of topological photonic devices that offer reliable directional transmissions

† z.lan@ucl.ac.uk
* jiezhu@tongji.edu.cn
§ zhongqing.su@polyu.edu.hk

and radiations.

1. Introduction

The emergence of photonic topological insulators (PTIs) offers numerous opportunities for controlling light with high efficiency and robustness [1]. Motivated by the various topological states in condensed matter physics, PTIs based on quantum Hall effect [2,3], quantum spin Hall effect [4-7] or quantum valley Hall effect [8-13] have been hitherto implemented. These PTIs obey the conventional bulk-boundary correspondence principle and host gapless topological edge states that are immune to defects and impurities in the bulk.

Recently, a new kind of PTI, the high-order PTI, has been proposed [14]. In a two-dimensional system, the high-order PTI is also referred to as the second-order PTI (SPTI), which hosts gapped edge states and in-gap corner states. Engineering the lattice symmetry plays a vital role in designing SPTI. To date, several modalities of SPTIs have been achieved in various lattices with different symmetries, such as square lattice with C_{4v} and C_4 symmetries [15-23], honeycomb lattice with C_{6v} symmetry [24,25], hexagonal lattice with C_3 symmetry [26-29] and so on. Despite a plenty of reported research on first-order and second-order PTIs, most of them only focus on the isotropic topological states formed between the topological trivial and nontrivial domains, whereas anisotropic topological states are rarely studied. In the seminal work attempting to achieve SPTIs based on the Su-Schrieffer-Heeger (SSH) model [15], Xie *et al.* discussed the anisotropic topological phases induced by an unequal coupling strength between the horizontal and vertical directions. However, the topological bandgap created by adjusting the distance between the dielectric cylinders on an empirical manner is small, and as such the resulting topological edge states are less localized. Om and Kim [30] discussed the second-order photonic topological phases of 2D photonic crystals (PCs) with L-shaped

anisotropic sublattice. Chen et al. [31] designed an acoustic frequency filter based on a 2D topological anisotropic phononic crystal. However, to date, only the anisotropic topological phase within the first-order bandgap was investigated for the transverse magnetic (TM) mode, leaving anisotropic topological phase within high-order bandgaps unexplored.

In this study, we explore the anisotropic topological phases within the odd-order bandgaps, from the first-order to the seventh-order of PCs, for both TM and transverse electric (TE) modes. PCs with extra-wide odd-order bandgaps are designed by the topology optimization method. By translating the primitive unit cell (UC) of the optimized PC along the horizontal direction by one half of the lattice constant, the anisotropic topological phase transition is realized. Highly localized anisotropic topological edge states are achieved at the interface between the primitive UCs and the translated UCs, which could find potential applications in the directional transport of light with robustness.

2. Results and discussions

Previous studies demonstrate that selecting unit cells from the same PC with odd-order band gap can lead to different topological properties [17,18,22,32]. To engineer anisotropic topological phases, first, we use the inverse design method to maximize the bandgap of the specific order, as described in Appendix A. The silicon with permittivity of $\varepsilon = 12$ is selected as the dielectric material of the PC. Figures 1 and 2 show the optimized PCs and their band diagrams with different odd-order bandgaps, from the first-order to the seventh-order, for the TM and the TE mode, respectively. The band diagrams are calculated by using COMSOL Multiphysics, wherein the unit cell is imposed with periodic boundary conditions. The dielectric materials form isolated rods for the TM mode and connecting walls for the TE mode. For brevity, the frequency herein is normalized with $\Omega = \omega a / 2\pi c$, where ω denotes the

angular frequency, a is the lattice constant, and c represents the speed of light. The midgap-gap-ratios of the optimized bandgaps for the PCs shown in Figs. 1 (a-d) are noted to be 39.2%, 36.51%, 31.78% and 45.64%, respectively, while these values are 30.7%, 29.0%, 31.4% and 46.4% for the PCs shown in Figs. 2 (a-d). These midgap-gap-ratios are significantly larger than those of traditional topological PCs from the two-dimensional (2D) SSH model [15], and thus are conducive to generating more localized topological modes.

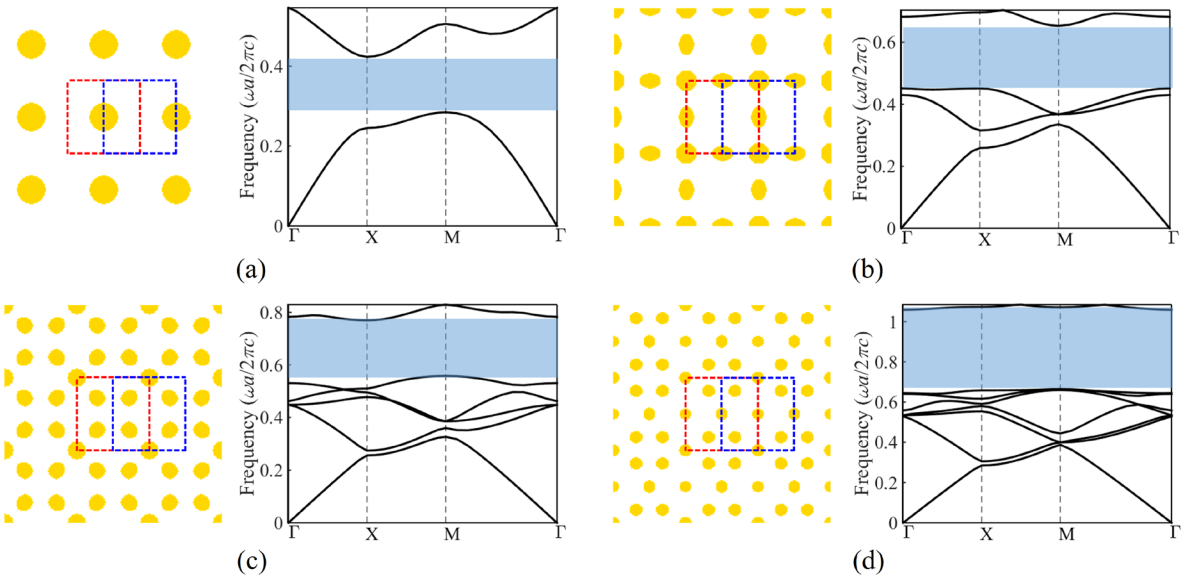

Fig. 1. The optimized PCs (3×3 unit cells) with different odd-order bandgaps for the TM modes, the schematic of the primitive UCs (red dashed boxes) and translated UCs (blue dashed boxes) and their band diagrams: (a) UCTM1A and UCTM1B with the first-order bandgap; (b) UCTM3A and UCTM3B with the third-order bandgap; (c) UCTM5A and UCTM5B with the fifth-order bandgap; (d) UCTM7A and UCTM7B with the seventh-order bandgap. The yellow color denotes the dielectric material.

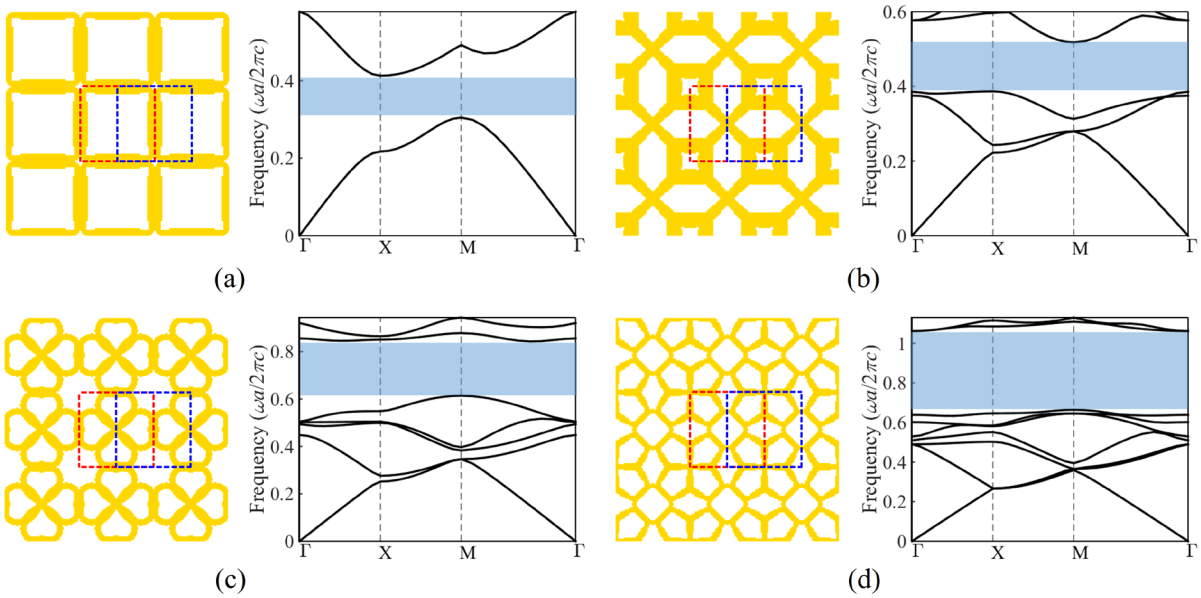

Fig. 2. The optimized PCs (3×3 unit cells) with different odd-order bandgaps for the TE modes, the schematic of the primitive UCs (red dashed boxes) and translated UCs (blue dashed boxes) and their band diagrams: (a) UCTE1A and UCTE1B with the first-order bandgap; (b) UCTE3A and UCTE3B with the third-order bandgap; (c) UCTE5A and UCTE5B with the fifth-order bandgap; (d) UCTE7A and UCTE7B with the seventh-order bandgap. The yellow color denotes the dielectric material.

Translating the primitive UC hosting odd-order bandgap by (a/2, a/2) changes the topological property of the band gap along both x and y directions, achieving isotropic topological phases [32]. Here, to construct the anisotropic topological phase, we translate the primitive UC by (a/2, 0). Such a translation only changes the topology property along the x-direction. The primitive UCs, denoted by the red dashed boxes in Figs. 1 and 2, are labeled with UCTMnA and UCTEnA, whereas the translated UCs, denoted by the blue dashed boxes, are labeled with UCTMnB and UCTEnB, respectively, where n denotes the order of the bandgap. Then, we adopt the 2D polarization $\mathbf{P}$=(P_x,P_y) to compute the topology properties of UCTMnA, UCTMnB, UCTEnA and UCTEnB, expressed by [33-35]

$$P_i = \frac{1}{2}\left(\sum_n q_i^n \text{modulo } 2\right), \qquad (-1)^{q_i^n} = \frac{\eta_n(\mathrm{X}_i)}{\eta_n(\Gamma)} \tag{1}$$

where *i* denotes the *x*- or *y*-direction. $\eta_n(\mathrm{X}_x)$, $\eta_n(\mathrm{X}_y)$ and $\eta_n(\Gamma)$ denote the parity ($\pm$) of the *n*th band at high symmetry points $\mathrm{X}\left(\frac{\pi}{a},0\right)$, $\mathrm{Y}\left(0,\frac{\pi}{a}\right)$ and Γ(0,0), respectively. The field profiles of corresponding eigenmodes can be used to determine the parity. The monopolar and quadrupolar modes have an even parity (+), whereas the dipolar mode possesses an odd parity (-). The $\sum_n q_i^n$ represents the summation of q over all bands below the bandgap.

The parities at X, Y and Γ of all bands below the bandgap for UCTM*n*A, UCTM*n*B, UCTE*n*A and UCTE*n*B are summarized in Appendix B. Because of the C_{4v} symmetry of UCTM*n*A and UCTE*n*A, $\eta_n(\mathrm{X}_x) = \eta_n(\mathrm{X}_y)$ for all of their bands. Substituting those parities into Eq. (1), we get that **P**=(0,0) for all UCTM*n*As and UCTE*n*As, indicating that they all host isotropic topological trivial phases. We can also achieve that **P**=(1/2, 0) for all UCTM*n*Bs and UCTE*n*Bs, suggesting that they all have anisotropic topological phases, i.e. topological nontrivial phases in the *x*-direction but topological trivial phases in the *y*-direction. As topological edge states appear at the interface between two domains of distinct topology properties, topological edge states are projected to arise on the *y*-direction boundary between UCTM*n*As (UCTE*n*As) and UCTM*n*Bs (UCTE*n*Bs), whereas they disappear on the *x*-direction boundary. Note that our numerical experiences indicate that translating the unit cell of PC with even-order band gap by (a/2, 0) could not change its topological property. Therefore, we only focus on exploring first-order topological phases with odd-order band gaps in this paper.

Two types of supercells consisting of six UCTM*n*As (UCTEnAs) and six UCTM*n*Bs

(UCTE*n*Bs) are developed to validate the above prediction based on the topology properties analysis, as illustrated in Figs. C1(a) and (b) in Appendix C, respectively. We designate the supercell (Fig. C1a) that consists of horizontally arranged UCTM*n*A (UCTE*n*A) and UCTM*n*B (UCTE*n*B) as STM*n*A (STE*n*A), and label the other supercell (Fig. C1b) that consists of vertically arranged UCTM*n*A (UCTE*n*A) and UCTM*n*B (UCTE*n*B) as STM*n*B (STE*n*B). Figures 3 and 4 show the calculated projected band structures of these supercells for TM and TE modes by using COMSOL Multiphysics, wherein the upper and bottom boundaries of STM*n*A(STE*n*A) and the left and right boundaries of STE*n*B(STE*n*B) are imposed with periodic boundary conditions. Topological edge states emerge within the bulk bandgaps for STM1A-STM7A and STE1A-STE7A with vertical interfaces (upper panels in Figs. 3 and 4). However, there are no topological edge states for STM1B-STM7B and STE1B-STE7B with horizontal interfaces (bottom panels in Figs. 3 and 4). For both TM and TE modes, these results confirm the anisotropic behavior of topological edge states created at the interfaces between the primitive UCs and the translated UCs. Note that topological edge states for STM1A-STM7A and STE1A-STE7A are all gapped, thus backscattering can be generated when they propagate with chirality [36]. In Appendix D, we further compare the localization degree of topological edge states for STM1B-STM7B with that of the supercell made of unit cells from Ref. [15], and one can find that the topological edge states for STM1B-STM7B are more localized.

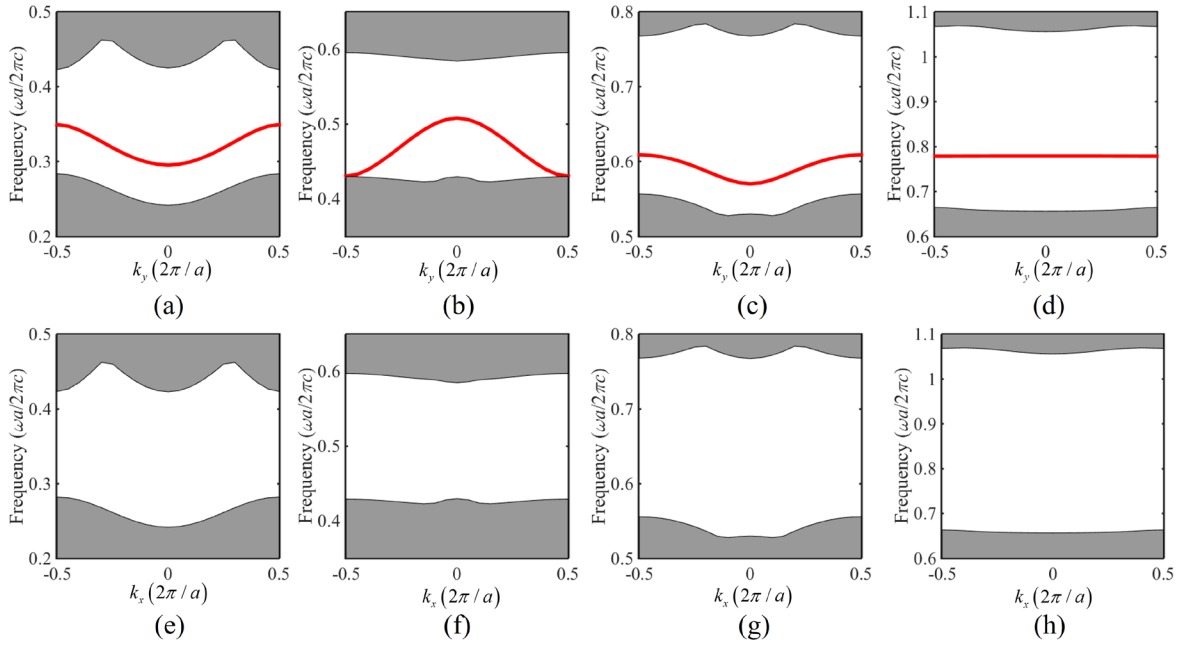

Fig. 3. Projected band diagrams for (a) STM1A, (b) STM3A, (c) STM5A, (d) STM7A, (e) STM1B, (f) STM3B, (g) STM5B and (h) STM7B.

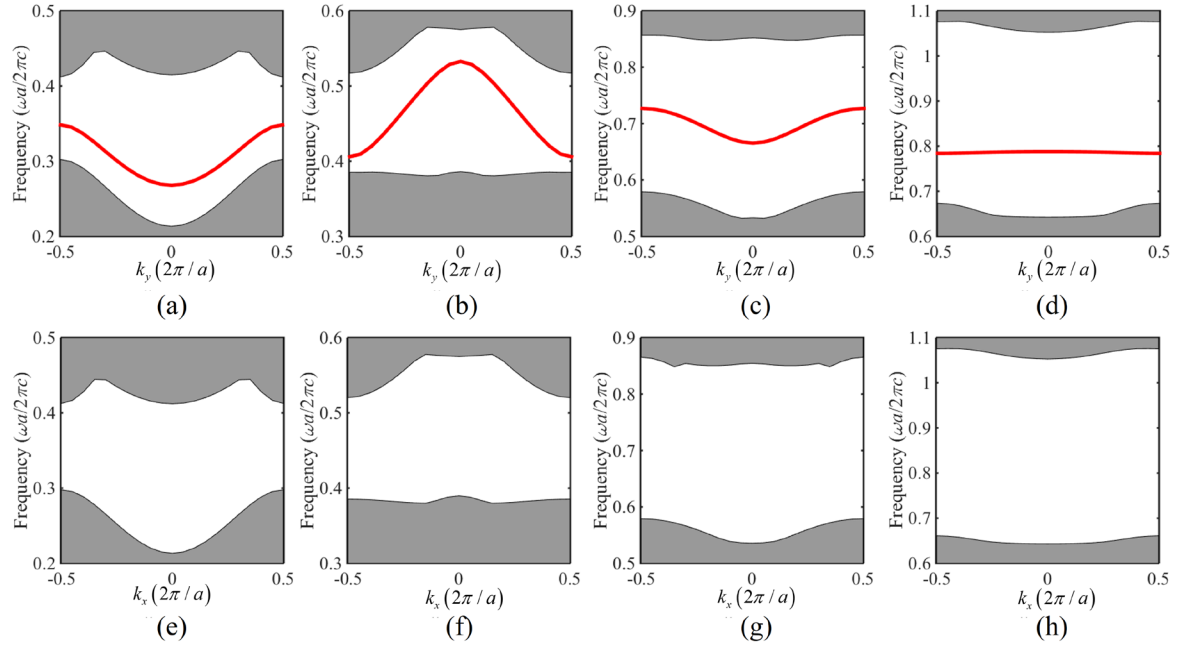

Fig. 4. Projected band diagrams for (a) STE1A, (b) STE3A, (c) STE5A, (d) STE7A, (e) STE1B, (f) STE3B, (g) STE5B and (h) STE7B.

To further demonstrate the transmission properties of these anisotropic topological edge states, we develop a metastructure consisting of 5×5 UCTM*n*Bs (UCTE*n*Bs) surrounded by three

layers of UCTM*n*As (UCTE*n*As), as sketched in Fig. C1(c) in Appendix C. The MTM*n* metastructure is made up of UCTM*n*A and UCTM*n*B, while the MTE*n* metastructure is made up of UCTE*n*A and UCTE*n*B. Next, we use COMSOL Multiphysics to calculate wave propagations in these metastructures. The source is placed in the corner indicated by the yellow ball [Fig. C1(c)] and the outer boundaries are set as scattering boundaries. Figures 5(a-d) show the electric field distributions for MTM1-MTM7 at excitation frequency of Ω = 0.32, 0.50, 0.60 and 0.78, respectively, which correspond to the topological edge states illustrated in Figs. 3(a-d). Figures 6(a-d) show the magnetic field distributions for MTE1-MTE7 at excitation frequency of Ω = 0.34, 0.48, 0.70 and 0.79, respectively, which correspond to the topological edge states illustrated in Figs. 4(a-d). It can be seen that waves can only propagate on the vertical border, whereas they are not allowed to propagate on the horizontal barrier. Such an anisotropic transmission feature could be useful in situations where directional transmission with robustness is required. Next, using MTM5 as an example, we introduce some defects by removing dielectric pillars within the blue dashed box [Fig. 7(a)] to show the robustness of the topological edge states. Figure 7(b) shows the electric field distribution at the excitation frequency of Ω =0.60 for MTM5 with defects. By comparing it with that for MTM5 without defects [Fig. 5(c)], we can find that the propagation of the wave along the boundary is not affected, validating the robustness of the topological edge state.

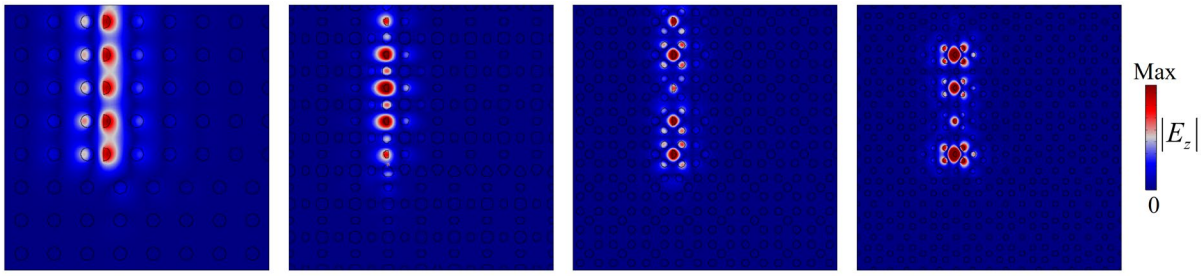

Fig. 5. Electric field distributions for (a) MTM1, (b) MTM3, (c) MTM5 and (d) MTM7 under the excitation frequency of Ω = 0.32, 0.50, 0.60, 0.78, respectively.

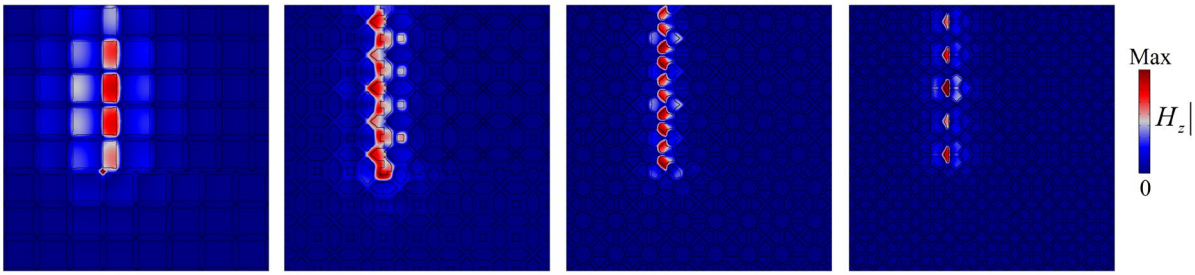

Fig. 6. Magnetic field distributions for (a) MTE1, (b) MTE3, (c) MTE5 and (d) MTE7 under the excitation frequency of Ω = 0.34, 0.48, 0.70 and 0.79, respectively.

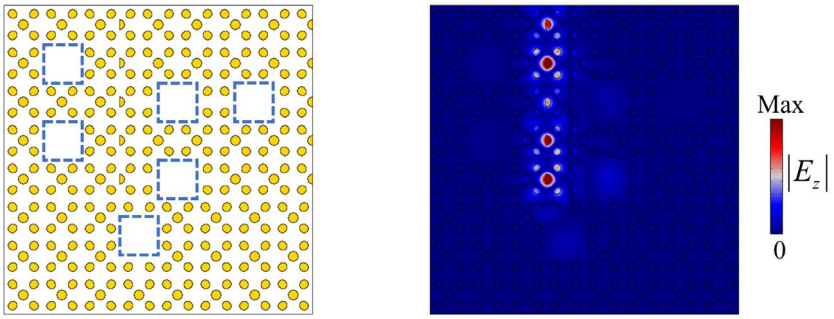

Fig. 7. Robustness of the anisotropic topological edge states. (a) Schematic of MTM5 with defects by removing dielectric pillars within the blue dashed box. (b) The electric field distribution at the excitation frequency of Ω =0.60.

3. Conclusions

To conclude, we establish anisotropic topological edge states in PCs for both TM and TE modes within odd-order bandgaps (from the first-order to the seventh-order). PCs with extra-wide odd-order bandgaps are designed using the topology optimization method. Anisotropic topological phase transition is achieved by translating the primitive UC of the optimized PC along the horizontal direction with half of the lattice constant. Tightly localized anisotropic topological edge states arise at the interface between the primitive UCs and the translated UCs. Full-wave simulations show that these topological states have anisotropic transmission features. Our findings could be used to create anisotropic topological photonic devices with reliable

directional light transmissions. In the future, designing PCs with several odd-order bandgaps to achieve multiple anisotropic topological edge states would also be interesting.

Appendix A: The inverse design method

In two-dimentional photonic crystals made of dielectric materials, the governing equation for TM and TE modes can be expressed by [37,38]

$$\text{TM: } -(\nabla + i\mathbf{k}) \cdot \left((\nabla + i\mathbf{k})E(\mathbf{r})\right) = \varepsilon(\mathbf{r}) \left(\frac{\omega}{c}\right)^2 E(\mathbf{r}) \tag{A1}$$

$$\text{TE: } -(\nabla + i\mathbf{k}) \cdot \left(\frac{1}{\varepsilon(\mathbf{r})}(\nabla + i\mathbf{k})H(\mathbf{r})\right) = \left(\frac{\omega}{c}\right)^2 H(\mathbf{r}) \tag{A2}$$

where $\mathbf{r}$ is the position vector. $E(\mathbf{r})$ and $H(\mathbf{r})$ denotes the the electric field and magnetic field for TM and TE modes, respectively. $\varepsilon(\mathbf{r})$ is the dielectric function. ω is the eigenfrequency. c is the speed of light. $\mathbf{k}=(k_x, k_y)$ is the wave vector.

We use the finite element method to solve Eqs. (A1) and (A2). We The discretize the domain into finite elements and assign each element with design variable x_e. Then we use the linear interpolation function to express the permittivity of design variable x_e:

$$\varepsilon(x_e) = \varepsilon_1(1 - x_e) + \varepsilon_2 x_e \tag{A3}$$

where ε_1 and ε_2 denote permittivities of air and dielectric material, respectively. In doing so, Eqs. (A1) and (A2) can be converted to a typical eigenvalue equation as

$$\left(\mathbf{K} - \left(\frac{\omega}{c}\right)^2 \mathbf{M}\right)\mathbf{u} = \mathbf{0} \tag{A4}$$

in which $\mathbf{K}$ and $\mathbf{M}$ are global matrixes and $\mathbf{u}$ is the eigenvector corresponding to the electric field for TM mode and magnetic field for TE mode.

The optimization objective is to maximize the odd-order band gap, expressed by

$$\max: f = 2\frac{\min\omega_{n+1}(\mathbf{k}) - \max\omega_n(\mathbf{k})}{\min\omega_{n+1}(\mathbf{k}) + \max\omega_n(\mathbf{k})} \tag{A5}$$

where n means band gap order.

Next, we derive the derivative of f with respect to x_e, which can be got after calculating $\frac{\partial \omega_n(\mathbf{k})}{\partial x_e}$ and $\frac{\partial \omega_{n+1}(\mathbf{k})}{\partial x_e}$. Differentiating both sides of Eq. (A4), $\frac{\partial \omega_n(\mathbf{k})}{\partial x_e}$ can be derived as

$$\frac{\partial \omega_n(\mathbf{k})}{\partial x_e} = \frac{1}{2\omega} \mathbf{u}^T \left(c^2 \frac{\partial \mathbf{K}}{\partial x_e} - \omega^2(\mathbf{k}) \frac{\partial \mathbf{M}}{\partial x_e} \right) \mathbf{u} \tag{A6}$$

Upon obtaining the the derivative of f with respect to x_e, the method of moving asymptotes (MMA) [39,40] is ultilized to update the design variables iteratively to maximize the objective function f.

Appendix B: Parities at high-symmetry points Γ, X and Y for UCTM*n*A, UCTE*n*A, UCTM*n*B and UCTE*n*B.

Tables B1 and B2 give the parities at high symmetry points X and Γ of bands below the designed bandgap for UCTM*n*A and UCTE*n*A. Note that, as UCTM*n*A and UCTE*n*A have C_{4v} symmetry, the parities at high symmetry points X and Y are identical. Tables B3 and B4 give the parities at high symmetry points X, Y and Γ of bands below the designed bandgap for UCTM*n*B and UCTE*n*B. The parities with opposites signs are shaded with blue colors, which can be taken into Eq. (1) to identify the topological properties.

Table B1. Parities at high symmetry points Γand X of the band structure of UCTM*n*A

Band order	UCTM1A		UCTM3A		UCTM5A		UCTM7A	
	Γ	X	Γ	X	Γ	X	Γ	X
1	+	+	+	-	+	+	+	+
2			+	+	-	-	+	-
3			+	-	-	+	-	-
4					+	-	-	-
5					+	+	+	+
6							+	+
7							+	-

Table B2. Parities at high symmetry points Γ and X of the band structure of UCTE*n*A

Band order	UCTE1A		UCTE3A		UCTE5A		UCTE7A	
	Γ	X	Γ	X	Γ	X	Γ	X
1	+	+	+	-	+	+	+	+
2			+	+	+	-	-	-
3			+	-	-	+	-	-
4					-	+	+	-
5					+	-	+	+
6							+	+
7							+	-

Table B3. Parities at high symmetry points X, Y and Γ of the band structure of UCTM*n*B

Band order	UCTM1B				UCTM3B				UCTM5B				UCTM7B			
	Γ	X	Γ	Y	Γ	X	Γ	Y	Γ	X	Γ	Y	Γ	X	Γ	Y
1	+	-	+	+	+	+	+	-	+	-	+	+	+	-	+	+
2					+	-	+	+	-	+	-	-	+	+	+	-
3					+	+	+	-	-	-	-	+	-	+	-	-
4									+	+	+	-	-	+	-	-
5									+	-	+	+	+	-	+	+
6													+	-	+	+
7													+	+	+	-

Table B4. Parities at high symmetry points X, Y and Γ of the band structure of UCTE*n*B

Band order	UCTE1B				UCTE3B				UCTE5B				UCTE7B			
	Γ	X	Γ	Y	Γ	X	Γ	Y	Γ	X	Γ	Y	Γ	X	Γ	Y
1	+	-	+	+	+	+	+	-	+	-	+	+	+	-	+	+
2					+	-	+	+	+	+	+	-	-	+	-	-
3					+	+	+	-	-	-	-	+	-	+	-	-
4									-	-	-	+	+	+	+	-
5									+	+	+	-	+	-	+	+
6													+	-	+	+
7													+	+	+	-

Appendix C: Schematics of supercells for calculating topological edge states and the metastructure for demonstrating anisotropic transmissions

Figures C1(a) and (b) plot the sketch of the supercell for calculating edge states along *y*-direction and *x*-direction, respectively. Figure C1(c) plots the sketch of the metastructure for demonstrating anisotropic transmissions.

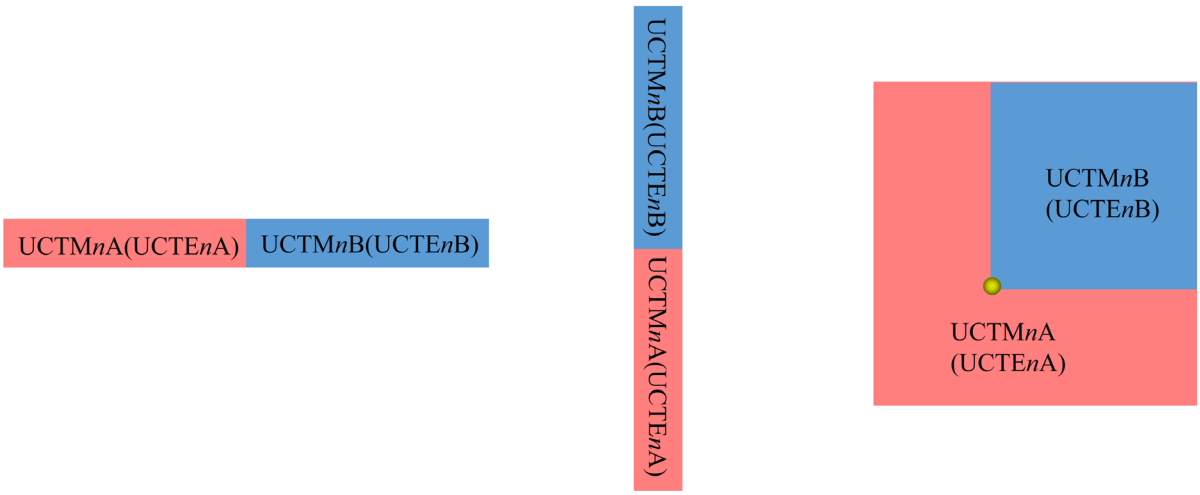

Fig. C1. (a,b) Sketch of the supercell for calculating topological edge states along (a) the *y*-direction and (b) the *x*-direction. (c) Sketch of the metastructure for the demonstration of anisotropic transmission.

Appendix D: Comparison of the localization degree of the topological edge states

Figure D1(a) shows the eigenfield of the topological edge state at k_y=0 for the supercell, which has the same size with STM*n*A, made of unit cells from Ref. [15], while Figs D1(b-e) present the eigenfields of edge states at k_y=0 for STM1A, STM3A, STM5A and STM7A, respectively. To compare the localization degree of the topological edge states, we set the left and right boundaries as scattering boundaries and calculate the quality factors of them. The quality factors are 2.4×10^3, 4.8×10^4, 5.5×10^9, 4.2×10^{14} and 3.9×10^{15} for the eigenfields in Figs. D1(a-e), respectively. We can find that the quality factors for STM1A- STM7A are significantly higher than that of the supercell made of unit cells from Ref. [15], meaning that the edge states of the supercells made of the optimized unit cells are more localized.

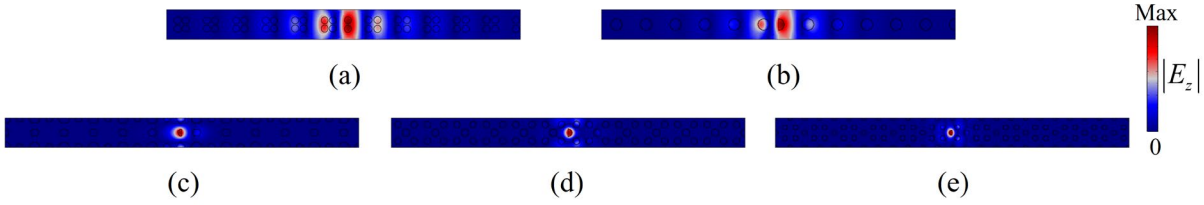

Fig. D1. Eigenfields of topological edge states at k_y=0 for (a) the supercell made of unit cells

from Ref. [15], (b) STM1A, (c) STM3A, (d) STM5A, (e) STM7A.

Acknowledgements

This work is supported by National Natural Science Foundation of China (No. 1210020421), the Hong Kong Scholars Program (No. XJ2020004), the Natural Science Foundation of Hunan Province (2022JJ40026), the Fundamental Research Funds for the Central Universities (Grant No. 22120220237) and the Research Grants Council of Hong Kong SAR (Grant No. AoE/P-502/20, 15205219).

References

[1] A. B. Khanikaev and G. Shvets, Nature Photonics **11**, 763 (2017).
[2] F. Haldane and S. Raghu, Physical review letters **100**, 013904 (2008).
[3] S. Raghu and F. D. M. Haldane, Physical Review A **78**, 033834 (2006).
[4] L.-H. Wu and X. Hu, Physical review letters **114**, 223901 (2015).
[5] D. Smirnova, S. Kruk, D. Leykam, E. Melik-Gaykazyan, D.-Y. Choi, and Y. Kivshar, Physical Review Letters **123**, 103901 (2019).
[6] Y. Chen, F. Meng, B. Jia, G. Li, and X. Huang, Physica Status Solidi-Rapid Research Letters **13**, 1900175 (2019).
[7] M. L. N. Chen, L. j. Jiang, Z. Lan, and W. E. I. Sha, IEEE Transactions on Antennas and Propagation **68**, 609 (2020).
[8] X.-T. He, E.-T. Liang, J.-J. Yuan, H.-Y. Qiu, X.-D. Chen, F.-L. Zhao, and J.-W. Dong, Nature Communications **10**, 872 (2019).
[9] X.-D. Chen, F.-L. Zhao, M. Chen, and J.-W. Dong, Physical Review B **96**, 020202 (2017).
[10] X. Ni, D. Purtseladze, D. A. Smirnova, A. Slobozhanyuk, A. Alù, and A. B. Khanikaev, Science advances **4**, eaap8802 (2018).
[11] M. Saba, S. Wong, M. Elman, S. S. Oh, and O. Hess, Physical Review B **101**, 054307 (2020).
[12] Y. Zeng *et al.*, Nature **578**, 246 (2020).
[13] Z. Lan, J. W. You, Q. Ren, W. E. I. Sha, and N. C. Panoiu, Physical Review A **103**, L041502 (2021).
[14] B. Xie, H.-X. Wang, X. Zhang, P. Zhan, J.-H. Jiang, M. Lu, and Y. Chen, Nature Reviews Physics **3**, 520 (2021).
[15] B.-Y. Xie, H.-F. Wang, H.-X. Wang, X.-Y. Zhu, J.-H. Jiang, M.-H. Lu, and Y.-F. Chen, Physical Review B **98**, 205147 (2018).
[16] B.-Y. Xie, G.-X. Su, H.-F. Wang, H. Su, X.-P. Shen, P. Zhan, M.-H. Lu, Z.-L. Wang, and Y.-F. Chen, Physical Review Letters **122**, 233903 (2019).
[17] Y. Chen, F. Meng, Z. Lan, B. Jia, and X. Huang, Physical Review Applied **15**, 034053 (2021).
[18] Y. Chen, Z. Lan, J. Li, and J. Zhu, Physical Review B **104**, 155421 (2021).
[19] Y. Ota, F. Liu, R. Katsumi, K. Watanabe, K. Wakabayashi, Y. Arakawa, and S. Iwamoto, Optica **6**, 786 (2019).
[20] X.-D. Chen, W.-M. Deng, F.-L. Shi, F.-L. Zhao, M. Chen, and J.-W. Dong, Physical Review Letters **122**, 233902 (2019).

[21] R. Gong, M. Zhang, H. Li, and Z. Lan, Optics Letters **46**, 3849 (2021).
[22] Y. Chen, Z. Lan, and J. Zhu, Physical Review Applied **17**, 054003 (2022).
[23] Y.-F. Gao, Y.-H. He, A. Maimaiti, M.-C. Jin, Y. He, and X.-F. Qi, Optics & Laser Technology **155**, 108387 (2022).
[24] B. Xie *et al.*, Nature Communications **11**, 3768 (2020).
[25] Y. Chen, F. Meng, Y. Kivshar, B. Jia, and X. Huang, Physical Review Research **2**, 023115 (2020).
[26] H.-X. Wang, L. Liang, B. Jiang, J. Hu, X. Lu, and J.-H. Jiang, Photonics Research **9**, 1854 (2021).
[27] Y. Chen, F. Meng, J. Zhu, and X. Huang, Applied Mathematical Modelling **102**, 194 (2022).
[28] O. Kang-Hyok and K.-H. Kim, Optics & Laser Technology **147**, 107616 (2022).
[29] K.-H. O and K.-H. Kim, physica status solidi (b) **259**, 2100568 (2022).
[30] K.-K. Om and K.-H. Kim, physica status solidi (b) **258**, 2100202 (2021).
[31] Z.-G. Chen, J. Zhao, J. Mei, and Y. Wu, Scientific reports **7**, 15005 (2017).
[32] Y. Chen, Z. Lan, and J. Zhu, Nanophotonics **11**, 1345 (2022).
[33] F. Liu, H.-Y. Deng, and K. Wakabayashi, Physical Review Letters **122**, 086804 (2019).
[34] Z. Zhang, M. R. López, Y. Cheng, X. Liu, and J. Christensen, Physical review letters **122**, 195501 (2019).
[35] Z. Zhang, H. Long, C. Liu, C. Shao, Y. Cheng, X. Liu, and J. Christensen, Advanced Materials **31**, 1904682 (2019).
[36] X. Zhang, H.-X. Wang, Z.-K. Lin, Y. Tian, B. Xie, M.-H. Lu, Y.-F. Chen, and J.-H. Jiang, Nature Physics **15**, 582 (2019).
[37] F. Meng, X. Huang, and B. Jia, Journal of Computational Physics **302**, 393 (2015).
[38] Y. Chen, F. Meng, G. Li, and X. Huang, Smart Materials and Structures **28**, 015025 (2018).
[39] J. Nocedal and S. J. Wright, *Numerical Optimization* (Springer, 1999).
[40] K. Svanberg, *A class of globally convergent optimization methods based on conservative convex separable approximations* (Society for Industrial and Applied Mathematics, 2002).